Combustion and Flame 225 (2021) 444–452

Contents lists available at ScienceDirect

Combustion and Flame

journal homepage: www.elsevier.com/locate/combustflame

Modeling third-body effects in the thermal decomposition of H_2O_2

Akira Matsugi

National Institute of Advanced Industrial Science and Technology (AIST), 16-1 Onogawa, Tsukuba 305-8569, Ibaraki, Japan

ARTICLE INFO

Article history:
Received 24 September 2020
Revised 12 November 2020
Accepted 13 November 2020
Available online 27 November 2020

Keywords:
Unimolecular reaction
Hydrogen peroxide
Third-body effect
Classical trajectory
Master equation

ABSTRACT

The thermal decomposition of hydrogen peroxide (H_2O_2) in seven bath gases (M = He, Ar, H_2, N_2, CO, CH_4, and H_2O) has been studied by classical trajectory calculations of the collisional energy transfer processes and master equation analyses of the pressure-dependent rate constants. The energy transfer processes are modeled with the range parameter of the exponential down model and collision frequency for energy transfer. Both of the two quantities are calculated from the collisional trajectories propagated on the potential energy surfaces directly evaluated by the optimized spin-component-scaled MP2 method. The master equation calculations using these parameters were found to give reasonable descriptions of the rate constants at low pressures. The calculated relative third-body efficiencies agree well with the available experimental data for M = He, Ar, and N_2 but the efficiency calculated for M = H_2O appears to be overestimated at low temperature. The calculated rate constants are represented by the limiting high-pressure rate constant of $k_\infty = 6.7 \times 10^{14}$ exp(−24800 K/T) s^{-1}, limiting low-pressure rate constants for M = Ar and N_2 of k_0(Ar) = 3.65×10^8 (T/K)$^{-4.691}$ exp(−26470 K/T) cm^3 $molecule^{-1}$ s^{-1} and $k_0(N_2) = 8.21 \times 10^9$ (T/K)$^{-5.034}$ exp(−26600 K/T) cm^3 $molecule^{-1}$ s^{-1}, the center broadening factor of $F_{cent} = 0.7$ exp(− T/3400 K), and the tabulated relative third-body efficiencies. The pressure-dependent rate constants calculated for multicomponent bath gases are reasonably reproduced by the traditional linear mixture rule, whereas the mixture rule based on the reduced pressure is found to provide a more precise description.

1. Introduction

An attempt is made to model the third-body effects in the kinetics of thermal decomposition of gaseous hydrogen peroxide (H_2O_2),

$$H_2O_2 + M \rightarrow OH + OH + M \quad (R1)$$

based on classical trajectory and master equation calculations. This reaction plays a key role in the degenerate chain branching process in combustion [1–4] and, therefore, detailed characterization of its temperature-, pressure-, and bath-gas-dependent rate constants is valuable for reliable kinetic modeling of relevant combustion processes.

Kinetics of the reaction R1 has been frequently studied in experiments using flow systems [5–8], static cells [9,10], and shock tubes [11–17]. Some theoretical studies have been reported on the decomposition and reverse recombination reactions [18–20], which employed empirically adjusted parameters to describe the collisional energy transfer and yielded the thermal rate constants over wide temperature and pressure ranges. Theoretical modeling of rate constants for unimolecular reactions requires characterization of the energy transfer processes in collisions with third-body molecules. Classical trajectory calculations have been used to study energy transfer processes (e.g., Refs. [21–35]), and recent efforts have shown that the trajectory-based master equation methods can reasonably describe pressure-dependent rate constants [28,30,33,35] and third-body efficiencies [34] in unimolecular reactions.

The present study aims to examine the feasibility of the classical trajectory and master equation methods for predicting the pressure-dependent kinetics and third-body effects on the title reaction. The energy transfer processes in collisions of H_2O_2 with third-body molecules are modeled based on the classical trajectory calculations. The rate constants for the H_2O_2 decomposition are calculated by solving master equations and compared with available experimental data. The calculations are carried out for the seven third-body molecules (M = He, Ar, H_2, N_2, CO, CH_4, and H_2O) to investigate the third-body effects, that is, the effects of different third-body molecules on the pressure-dependent rate constants. Another aim of the study is to evaluate the validity of rate constant expressions used in kinetic modeling studies. The third-body effects are in most cases described by the relative third-body efficiencies defined as the relative values of the limiting

E-mail address: a.matsugi@aist.go.jp

https://doi.org/10.1016/j.combustflame.2020.11.019
0010-2180/

low-pressure rate constants for third-body molecules, which are usually assumed to be independent of temperature. The pressure dependence of the rate constants is represented using the falloff expressions [36–38] whose parameters are generally assumed to be the same for all third-body molecules. Furthermore, the rate constants for multicomponent bath gases have been assumed to obey the traditional linear mixture rule, which is known to underestimate the rate constants [39–41] and can be a major source of uncertainties in rate constant representations [41]. These assumptions are hard to be assessed experimentally because of difficulties in measuring the rate constants in various bath gases over wide ranges of temperature and pressure. The present study addresses these common assumptions by computationally modeling the collisional energy transfer processes in a non-empirical way.

2. Computational methods

The trajectory calculations were carried out on full-dimensional potential energy surfaces (PESs) of the H_2O_2 + M systems for M = He, Ar, H_2, N_2, CO, CH_4, and H_2O. The method and procedure for the trajectory calculations are similar to those used in the previous studies [32–34]. Although these previous studies mainly employed the PESs calculated using the density-functional tight-binding (DFTB) method with some ad hoc corrections, the same method was found to be not suitable for describing the PES of H_2O_2; therefore, the second-order Møller–Plesset perturbation (MP2) theory was employed in the present study with some corrections for the correlation energies. As practiced in the previous study on C_2H_6 + Ar collisions [32], the spin components of the correlation energy were artificially scaled to yield the correlation energy (E_c) of the spin-component-scaled (SCS)-MP2 method [42] as

$$E_c = p_S E_S^{(2)} + p_T E_T^{(2)} \quad (1)$$

where $E_S^{(2)}$ and $E_T^{(2)}$ are the antiparallel- and parallel-spin pair contributions to the MP2 correlation energy, respectively, and p_S and p_T are scaling factors. Unlike the original SCS-MP2 method, the values of the two scaling factors were determined for each H_2O_2 + M system with specific basis sets in order to reasonably describe both intramolecular and interaction PESs in a cost-effective manner. Hereafter, the method is denoted as SCS′-MP2 to indicate the use of nonstandard scaling factors. The basis sets used were 6–31G(d), 6–31+G(d,p), and aug-cc-pVDZ, depending on M, as described later.

The optimal values of the scaling factors, p_S and p_T, were derived by comparing the SCS′-MP2 energies to the reference energies obtained using the explicitly correlated coupled-cluster method at the CCSD(T)-F12a/aug-cc-pVTZ level of theory [43,44]. The reference energies were calculated for 1000 sampled structures of isolated H_2O_2 molecules as well as ~2000 structures of the H_2O_2 + M interaction for each M. The intramolecular structures of H_2O_2 and M were sampled following the procedure for preparing initial structures of trajectories as described below. For the interaction, 100 different orientations were randomly generated for each M, and ~20 structures were obtained for each orientation by varying the center-of-mass distances between H_2O_2 and M from 10 to typically 1–3 Å where the repulsive interaction potential energy became ~50 kJ mol^{-1}. The MP2 and coupled-cluster calculations were performed using the Gaussian 09 [45] and Molpro 2018.2 [46] programs, respectively.

The trajectory calculations were performed at temperatures of T = 750 and 1500 K. The initial vibrational and rotational states of H_2O_2 were generated by classical microcanonical sampling with the vibrational energy of 200 kJ mol^{-1} above the zero-point level (≈268 kJ mol^{-1} above the potential minimum) and quasi-classical rigid-rotor sampling from a thermal distribution at temperature T, respectively [32,47]. The vibrational energy was selected to be close to the dissociation threshold energy. The rovibrational states of molecular colliders were generated from the thermal distributions by the quasi-classical normal-mode/rigid-rotor sampling method [47]. The relative velocities of the molecule and collider were determined from the relative translational energy sampled from the thermal distribution. Impact parameter b was uniformly sampled over the range 0–b_{max}, where the maximum impact parameter b_{max} was set to be $15a_0$, $20a_0$, $20a_0$, $30a_0$, $30a_0$, $40a_0$, and $60a_0$ for M = He, Ar, H_2, N_2, CO, CH_4, and H_2O, respectively, to obtain converged results, where a_0 is the Bohr radius. At each temperature, batches of 2000 (for M = He, Ar, H_2, and N_2), 1000 (for M = CO and CH_4), or 600 (for M = H_2O) trajectories were propagated directly on the SCS′-MP2 PES using the five-stage, fourth-order symplectic integrator [48] with a time step of 0.4 fs, which was found to be sufficient for conserving the total energy within much less than 1 cm^{-1} during each trajectory.

The rate constants for the thermal decomposition of H_2O_2 were calculated by solving the one-dimensional master equation formulated as a function of the total rovibrational energy, E. Although accurate a priori modeling of the collision processes requires an explicit two-dimensional formulation of the master equation as a function of E and the total angular momentum J [27,30,35], a simple one-dimensional variant was employed here because the present trajectory results are not statistically sufficient for characterizing the E- and J-resolved collisional transitions, especially for the polyatomic third bodies. The collisional energy transfer process is modeled by the collision frequency, Z, and probability function $P(E, E')$ for collisional transitions from energies E' to E. The exponential down model [49]

$$P(E, E') \propto \exp\left(-\frac{E'-E}{\alpha}\right) \quad (2)$$

is employed for deactivating ($E' > E$) collisions, where the parameter α corresponding to the average energy transferred in deactivating collisions. The probabilities for activating transitions are determined by detailed balance.

The values of the parameter α and collision frequency Z can be derived from the results of the trajectory calculations as [32]

$$\ln\alpha = \frac{\sum_{i=1}^{N_d} w_i(E_i'-E_i)\ln(E_i'-E_i)}{\sum_{i=1}^{N_d} w_i(E_i'-E_i)} - \psi(2) \quad (3)$$

$$Z = \frac{\sum_{i=1}^{N_d} w_i(E_i'-E_i)}{\alpha}\pi b_{max}^2\sqrt{8k_BT/\pi\mu} \quad (4)$$

where E_i' and E_i are the pre- and post-collision rovibrational energies of H_2O_2, respectively, for the ith deactivating trajectory, N_d is the number of trajectories leading to deactivation, w_i is the weighting factor for correcting for bias in the sampling of impact parameter, ψ is the digamma function, k_B is the Boltzmann constant, and μ is the reduced mass of H_2O_2 and M. These expressions can correctly model the first-order moment of the energy transfer and the derivative of the moment at the first order [32–34], both of which are important quantities for describing the kinetics of unimolecular reactions at low pressures [32]. All error limits reported for quantities derived from the trajectory calculations correspond to two standard errors estimated by the bootstrapping method [35,50].

The density of states of H_2O_2 was calculated by the modified Beyer-Swinehart algorithm [49] using the fundamental frequencies (877, 1266, 1402, 3599, and 3608 cm^{-1}) [51], rotational constants (10.3560, 0.8656, and 0.8270 cm^{-1}) [51], and the energy levels for the torsional mode (numerically calculated by the BEx1D program [52] using the torsional potential given in Ref. [53]). The micro-

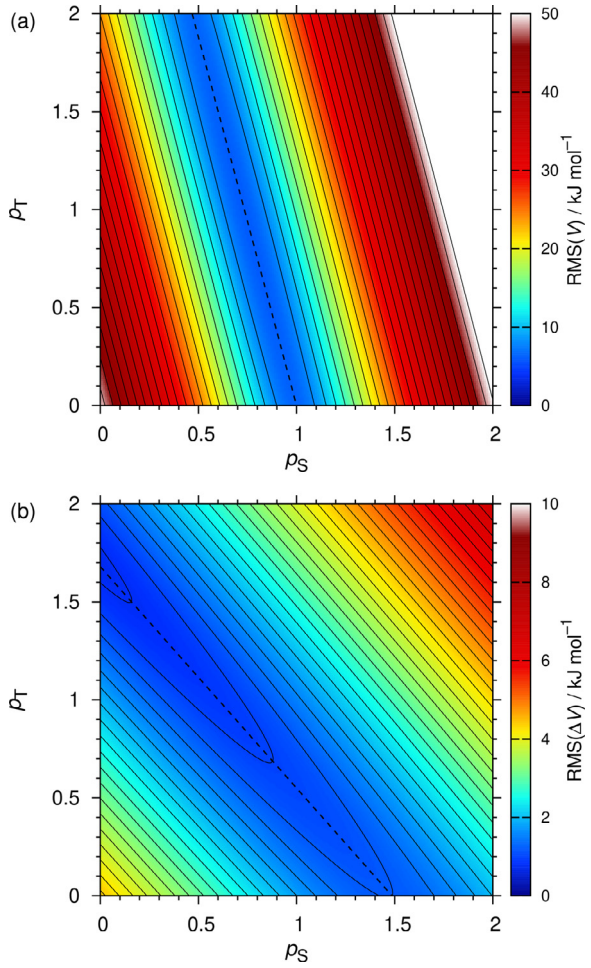

Fig. 1. RMS deviations between the SCS′-MP2/6-31G(d) and CCSD(T)-F12a/aug-cc-pVTZ energies for (a) H_2O_2 and (b) interaction between H_2O_2 and N_2 plotted as functions of p_S and p_T. Contour increments are 2 and 0.2 kJ mol^{-1} for V and ΔV, respectively. The dashed lines represent valley lines.

canonical rate constants, $k(E)$, were calculated by inverse Laplace transform method [54] using the limiting high-pressure rate constant represented by

$$k_\infty = 6.7 \times 10^{14} \exp(-24800\,\mathrm{K/T})\ \mathrm{s}^{-1} \quad (5)$$

which was derived from the rate constant for the reverse reaction, 2.4×10^{-11} $(T/300\ \mathrm{K})^{-0.5}$ cm^3 molecule^{-1} s^{-1} [55], and the equilibrium constant [20].

3. Results and discussion

3.1. Potential energy surface

The scaling factors, p_S and p_T, for SCS′-MP2 correlation energies were obtained by minimizing the root mean square (RMS) deviations between the SCS′-MP2 energies and those calculated at the CCSD(T)-F12a/aug-cc-pVTZ level for the sampled H_2O_2 and H_2O_2 + M structures. Because the optimal values of p_S and p_T differ for intramolecular and interaction potentials, their values were determined by the following procedure. Figure 1 shows contour plots of the RMS deviations for the intramolecular (V) and interaction (ΔV) potential energies for M = N_2 as functions of p_S and p_T, where V is the potential energy of H_2O_2 relative to its minimum and ΔV is defined as the potential energy of H_2O_2 + M relative to that at infinite separation between H_2O_2 and M. The SCS′-MP2 energies were calculated with the 6-31G(d) basis set. The contour plots for V and ΔV exhibit different trends with respect to the scaling factors. The dashed lines on the contour maps are the valley lines, which are drawn to cross the contour lines at right angles. The valley lines for the RMS deviations in V and ΔV have different slopes. The values of p_S and p_T were selected as a point at the intersection of the two valley lines, which gives a balanced description of both intramolecular and intermolecular potentials. The valley lines for ΔV depend on the third-body molecule, and the scaling factors were determined for each M in the same manner.

The obtained scaling factors are listed in Table 1. The 6-31G(d) basis set is employed for M = Ar, N_2, CO, and CH_4. For M = He and H_2, the 6-31+G(d,p) basis set is employed because the use of the 6-31G(d) basis set resulted in unphysical negative values of p_S. The interaction of H_2O_2 with M = H_2O is a more difficult case; the basis sets such as 6-31G(d) and 6-31+G(d,p) gave significantly larger RMS deviations in ΔV than those listed in Table 1, and a much larger aug-cc-pVDZ basis set had to be adopted to obtain reasonably small deviations. The RMS and mean absolute (MA) deviations between the SCS′-MP2 and reference CCSD(T)-F12a/aug-cc-pVTZ energies are shown in Table 1. The deviations in the H_2O_2 intramolecular energies were a few percent of the excitation energy (≈268 kJ mol^{-1}). Recent studies [28,32] indicated that collisional energy transfer in highly excited polyatomic molecules is not strongly sensitive to the intramolecular potential, and the performance shown in Table 1 are considered sufficient for the present purpose. The RMS and MA deviations in the interaction potentials were 0.50–1.07 and 0.24–0.57 kJ mol^{-1}, respectively. These values are comparable to, or slightly better than, those in the previous study on CH_3NC + M [34], in which the trajectory calculations could reasonably reproduce the experimental relative third-body efficiencies for the thermal isomerization reaction.

3.2. Collisional energy transfer

The energy transfer parameters α and collision frequencies Z calculated form the trajectories and the limiting low-pressure rate constants k_0 calculated by solving the master equations are listed in Table 2. With the present ensemble sizes of the trajectories, the statistical uncertainties (two standard errors) in k_0 are better than 30% except for the ≈40% uncertainty for M = H_2O at 1500 K. Both α and Z depend sensitively on the type of the third-body molecule. The results indicate that the third-body efficiencies are governed primarily by the variation of the collision frequencies among the different bath gas molecules, though the variation of α is also important for quantitative calculations. This observation is consistent with the previous study on CH_3NC + M [34].

The collision frequencies are compared with the Lennard-Jones (LJ) collision frequencies, Z_{LJ}, and capture rate constants, Z_{cap}, in Table 3, where the relative values, Z/Z_{LJ} and Z/Z_{cap}, are listed. The angle-averaged reduced collision integrals were used in the calculation of Z_{LJ} for polar colliders [34,56,57]. The capture rate constants were calculated for isotropic dispersion interaction potentials [32] even for polar colliders because the contribution of the dipole-dipole interaction to the capture rates is minor at high temperatures. The LJ parameters and dipole moments were taken from the literature [58,59]. The calculated collision frequencies are substantially larger than Z_{LJ} and Z_{cap}, except that Z is close to Z_{cap} for monatomic colliders. This trend is similar to those observed in the previous studies [32,34], and the nature of the long-range interaction between H_2O_2 and M is the main factor controlling the collision frequency for energy transfer; in particular, the large value of Z for M = H_2O is considered to be caused by the anisotropy [34] of the dipole-dipole interaction between H_2O_2 and H_2O.

Table 1
Basis sets and scaling factors for SCS′-MP2 calculations and RMS and MA deviations between the SCS′-MP2 and CCSD(T)-F12a/aug-cc-pVTZ intramolecular (V) and interaction (ΔV) energies (in units of kJ mol^{-1}).

M	basis set	p_S	p_T	RMS(V)	MA(V)	RMS(ΔV)	MA(ΔV)
He	6-31+G(d,p)	0.00	3.98	8.4	6.5	0.50	0.24
Ar	6-31G(d)	0.17	3.12	7.9	5.9	0.86	0.41
H_2	6-31+G(d,p)	0.36	2.77	7.0	5.6	0.83	0.41
N_2	6-31G(d)	0.78	0.82	6.1	4.7	0.97	0.49
CO	6-31G(d)	0.75	0.94	6.1	4.7	0.89	0.50
CH_4	6-31G(d)	0.45	2.06	6.7	5.1	1.07	0.57
H_2O	aug-cc-pVDZ	0.76	1.14	3.6	2.9	0.51	0.32

Table 2
Calculated energy transfer parameters α, collision frequencies Z, and limiting low-pressure rate constant k_0.

T (K)	M	α (cm^{-1})	Z (cm^3 molecule^{-1} s^{-1})	k_0 (cm^3 molecule^{-1} s^{-1})
750	He	211 ± 32	(8.72 ± 0.83) × 10^{-10}	(4.49 ± 0.89) × 10^{-21}
750	Ar	305 ± 46	(6.26 ± 0.72) × 10^{-10}	(5.44 ± 0.92) × 10^{-21}
750	H_2	178 ± 23	(3.03 ± 0.24) × 10^{-9}	(1.20 ± 0.20) × 10^{-20}
750	N_2	262 ± 40	(1.49 ± 0.16) × 10^{-9}	(1.05 ± 0.20) × 10^{-20}
750	CO	308 ± 71	(1.67 ± 0.20) × 10^{-9}	(1.46 ± 0.36) × 10^{-20}
750	CH_4	515 ± 108	(2.24 ± 0.27) × 10^{-9}	(3.67 ± 0.78) × 10^{-20}
750	H_2O	618 ± 159	(5.31 ± 0.75) × 10^{-9}	(1.05 ± 0.22) × 10^{-19}
1500	He	342 ± 61	(1.08 ± 0.12) × 10^{-9}	(9.72 ± 2.14) × 10^{-15}
1500	Ar	481 ± 83	(6.65 ± 0.85) × 10^{-10}	(1.03 ± 0.23) × 10^{-14}
1500	H_2	276 ± 42	(3.32 ± 0.32) × 10^{-9}	(2.10 ± 0.42) × 10^{-14}
1500	N_2	352 ± 69	(1.82 ± 0.23) × 10^{-9}	(1.72 ± 0.42) × 10^{-14}
1500	CO	454 ± 94	(1.99 ± 0.21) × 10^{-9}	(2.81 ± 0.79) × 10^{-14}
1500	CH_4	528 ± 135	(2.79 ± 0.41) × 10^{-9}	(4.95 ± 1.49) × 10^{-14}
1500	H_2O	448 ± 161	(8.40 ± 1.88) × 10^{-9}	(1.16 ± 0.48) × 10^{-13}

Table 3
Comparison of collision frequencies.

M	Z/Z_{LJ} (750 K)	Z/Z_{LJ} (1500 K)	Z/Z_{cap} (750 K)	Z/Z_{cap} (1500 K)
He	1.48 ± 0.14	1.43 ± 0.16	1.03 ± 0.10	1.13 ± 0.12
Ar	1.52 ± 0.17	1.29 ± 0.16	0.88 ± 0.10	0.83 ± 0.11
H_2	3.00 ± 0.23	2.60 ± 0.25	1.79 ± 0.14	1.74 ± 0.17
N_2	3.18 ± 0.34	3.09 ± 0.39	1.87 ± 0.20	2.04 ± 0.26
CO	3.56 ± 0.43	3.39 ± 0.36	2.06 ± 0.25	2.19 ± 0.23
CH_4	3.77 ± 0.45	3.78 ± 0.55	2.12 ± 0.25	2.35 ± 0.34
H_2O	8.92 ± 1.25	13.0 ± 2.9	5.32 ± 0.75	7.50 ± 1.68

3.3. Rate constants

The temperature- and pressure-dependent rate constants for M = Ar and N_2 are calculated by solving the master equation using the temperature-dependent parameters, α and Z, derived by interpolating the trajectory results as α = 369 (T/1000 K)$^{0.655}$ cm^{-1} and Z = 6.42 × 10^{-10} (T/1000 K)$^{0.087}$ cm^3 molecule^{-1} s^{-1} for M = Ar and α = 296 (T/1000 K)$^{0.423}$ cm^{-1} and Z = 16.2 × 10^{-10} (T/1000 K)$^{0.289}$ cm^3 molecule^{-1} s^{-1} for M = N_2. Figure 2 shows the calculated limiting low-pressure rate constants, k_0, and the second-order rate constants, k_{2nd}, at a pressure of 2 bar. The reported experimental rate constants [5,7,8,13–17] are also plotted for comparison. The calculated second-order rate constants at 2 bar show only a slight deviation from the limiting low-pressure rate constants; therefore, the experimental data plotted here are expected to be close to the low-pressure limit. The calculated rate constants are in excellent agreement with the experimental values reported over several orders of magnitude. It should be noted that such excellent agreement is potentially attributed to fortuitous cancellation of errors arising from several factors such as uncertainty in the parameters derived from the trajectory calculation, effect of the angular momentum conservation, and vibrational anharmonicity. The calculated limiting low-pressure rate constants for M = Ar and N_2 over the extrapolated temperature range of 500–2000 K are represented as

$$k_0(\mathrm{Ar}) = 3.65 \times 10^8 (T/\mathrm{K})^{-4.691} \exp(-26470\,\mathrm{K}/T)\ \mathrm{cm^3\ molecule^{-1}\ s^{-1}} \quad (6)$$

and

$$k_0(\mathrm{N_2}) = 8.21 \times 10^9 (T/\mathrm{K})^{-5.034} \exp(-26600\,\mathrm{K}/T)\ \mathrm{cm^3\ molecule^{-1}\ s^{-1}} \quad (7)$$

with the precision better than ±5%. The statistical uncertainties in the calculated values of k_0 are approximately ±20% for these bath gases.

The pressure dependence of the rate constants has been reported in some shock tube studies [13,14,16] up to a pressure of 15 bar, which is compared with the calculated rate constants in Fig. 3. The calculated values are within the scatter of the experimental rate constants except at the highest temperature (1250 K) and high pressures (≥10 bar) where the experimental data are systematically smaller than the master equation prediction. Similar deviations were reported in the previous master equation study of Sellevåg et al. [19] and fall-off modeling of Troe [20]. There is at present no rational explanation for these deviations. Given that the deviations are seen only at the high temperature and pressure, there might be some overestimation of the microscopic rate constants at high energies as well as a possibility of non-statistical behavior in the dissociation [18,20]. The present microscopic rate constants are calculated by the inverse Laplace transform method, and their energy dependence originates from the presumed temperature dependence of $T^{-0.5}$ in the limiting high-pressure rate constant for the reverse recombination reaction [55] as well as the temperature dependence of the equilibrium constant. This $T^{-0.5}$ dependence in the recombination rate constant was loosely based on the theoretical predictions of Sellevåg et al. [19] and Troe and Ushakov [18]; therefore, the deviations seen in the present and previous [19,20] studies may have the same origin. Experimen-

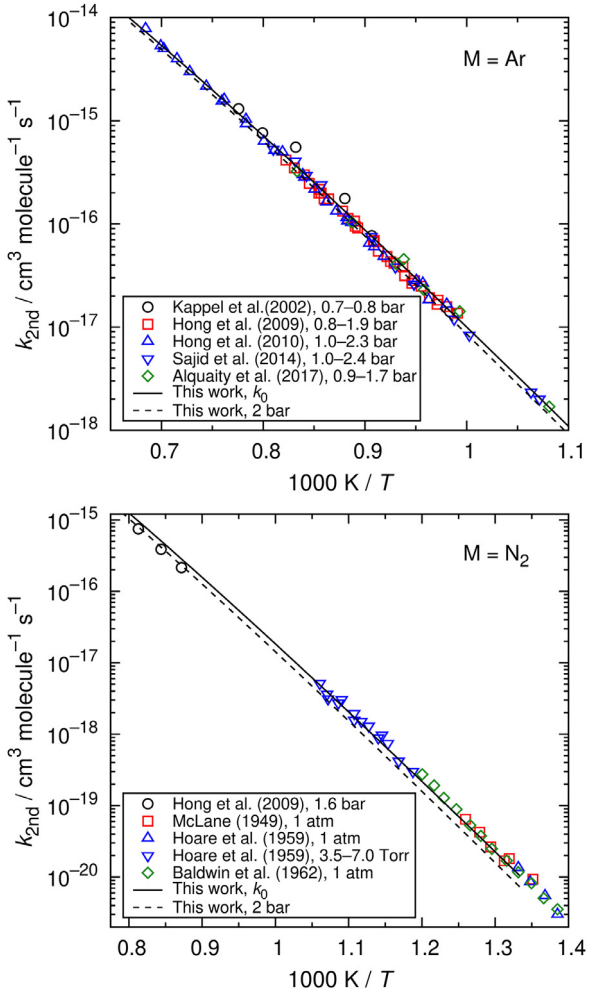

Fig. 2. Calculated (lines) and experimental [5,7,8,13–17] (symbols) second-order rate constants for the thermal decomposition of H_2O_2 in Ar (top) and N_2 (bottom) baths.

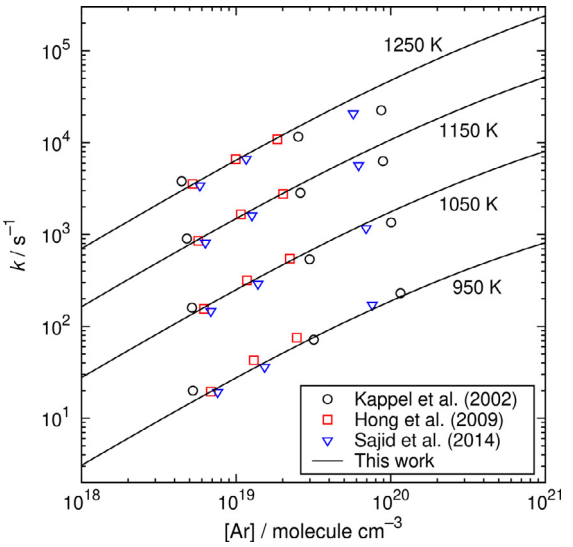

Fig. 3. Calculated (lines) and experimental [13,14,16] (symbols) pressure-dependent rate constants for the thermal decomposition of H_2O_2 in an Ar bath at temperatures of 950, 1050, 1150, and 1250 K from bottom to top.

tally, the two high-pressure measurements of the decomposition rate constants [13,16] showed a good agreement with each other despite the differences in the shock tube facilities and detection methods. The plotted high-pressure rate constants for T = 1250 K were derived by extrapolations using the Arrhenius equation from the data measured at lower temperatures, but the extrapolations are short and might not cause significant uncertainties. All the reported shock-tube experiments [11–17] consistently yielded an apparent activation energy of ≈180 kJ mol^{-1} at a pressure of ~1 bar. However, smaller apparent activation energies of 166 ± 2 and 161 ± 4 kJ mol^{-1} were reported at pressures of 10 and 15 bar, respectively [13,16], which contradict the expected positive pressure-dependence of the apparent activation energy. Further studies, both theoretical and experimental, are needed to resolve the discrepancy.

3.4. Third body effects

The calculated relative third-body efficiencies, defined as the ratios of the limiting low-pressure rate constants for the third body M, k_0(M), to that for M = N_2, $k_0(N_2)$, are listed in Table 4 together with the relative rate constants, k(M)/$k(N_2)$, calculated at pressures of 0.1 and 1 bar and the experimental values [7,8,10,14]. The calculated efficiencies are increasing in the order He ≈ Ar < N_2 ≈ H_2 < CO < CH_4 < H_2O, which is consistent with the orders observed in this and some other reaction systems (e.g., Refs. [60–63]). The pressure dependences of the relative rate constants are insignificant at these pressures except for CH_4 and H_2O. There appear to be some temperature dependencies in the relative efficiencies, but the differences between the values at 750 and 1500 K are within the statistical uncertainties. The relative efficiencies in the low-pressure limit can be alternatively calculated using the Troe's collision efficiency [64], $\beta_c \approx [\alpha/(\alpha + F_E k_B T)]^2$, derived from the approximate analytical solution to the one-dimensional master equation. The quantity F_E is an energy dependence factor of the density of states and F_E ≈ 1.1 and 1.3 for H_2O_2 at temperatures of 750 and 1500 K, respectively. The parameters α calculated from the trajectories result in the values of β_c ranging from 0.056 to 0.27 at 750 K and from 0.029 to 0.079 at 1500 K for the seven third-body molecules studied. The relative efficiencies estimated as the ratios of the values $Z\beta_c$ for M to that for M = N_2 are listed in Table 4, which accurately reproduce the relative rate constants calculated by numerically solving the master equations.

The calculated relative efficiencies are in good agreement with the experimental values for M = He and Ar. For M = H_2O, the experimental values of $k(H_2O)/k(N_2)$ measured at 707–919 K [7,8,10] are larger than the calculated relative rate constant at 750 K but rather close to that at 1500 K. Aside from experimental uncertainties, the deviation at the low temperature may potentially be caused by the neglect of the angular momentum conservation in the present master equation. The effect of the angular momentum conservation is expected to be significant for efficient colliders at low temperatures [29], and an explicit two-dimensional master equation modeling would be required for quantitative calculations; such calculations have not been carried out in the present study due to the reason mentioned above. Overall, except for this issue, the present calculations yielded the low-pressure rate constants and relative third-body efficiencies that are fairly consistent with the available experimental data.

The experimental data are available also for the other third-body molecules, M = O_2, CO_2, and H_2O_2. The calculation for M = O_2 could not be carried out because there were convergence problems in the molecular orbital calculations at some regions of the potential energy surface. Preliminary calculations for M = CO_2 using the 6-31G(d) basis set indicated the efficiency of ~1.5 relative to M = N_2, which appears to be close to the experimental

Table 4
Calculated and reported relative rate constants, $k(M)/k(N_2)$.

M	750 K, $Z\beta_c$[a]	750 K, LPL[b]	750 K, 0.1 bar	750 K, 1 bar	1500 K, $Z\beta_c$[a]	1500 K, LPL[b]	1500 K, 0.1 bar	1500 K, 1 bar	experiment
He	0.43 ± 0.13	0.43 ± 0.12	0.43 ± 0.12	0.47 ± 0.12	0.56 ± 0.19	0.57 ± 0.18	0.57 ± 0.19	0.58 ± 0.19	0.57[c], 0.53[d]
Ar	0.51 ± 0.15	0.52 ± 0.13	0.53 ± 0.13	0.57 ± 0.13	0.60 ± 0.20	0.59 ± 0.19	0.60 ± 0.20	0.62 ± 0.20	0.67[e], 0.67[f]
H_2	1.15 ± 0.33	1.14 ± 0.29	1.12 ± 0.28	1.08 ± 0.25	1.22 ± 0.38	1.23 ± 0.38	1.21 ± 0.38	1.19 ± 0.36	
CO	1.38 ± 0.48	1.39 ± 0.43	1.38 ± 0.42	1.34 ± 0.38	1.63 ± 0.61	1.62 ± 0.60	1.63 ± 0.60	1.60 ± 0.58	
CH_4	3.41 ± 1.06	3.48 ± 0.99	3.35 ± 0.93	2.92 ± 0.73	2.88 ± 1.11	2.83 ± 1.05	2.85 ± 1.10	2.72 ± 1.02	
H_2O	9.72 ± 3.08	9.98 ± 2.78	8.78 ± 2.37	6.21 ± 1.47	6.76 ± 3.12	6.70 ± 3.22	6.47 ± 3.07	5.72 ± 2.59	4.0[c], 4.3[d], 6.0[e]
O_2									0.71[d], 0.78[e]
CO_2									1.24[d]
H_2O_2									5.4[c], 5.9[d], 6.6[e]

[a] Calculated as the ratio of $Z\beta_c$.
[b] Low-pressure limit.
[c] Ref. [10] (707 K, <100 Torr); the values were converted using the efficiency for oxygen [8].
[d] Ref. [7] (919 K, ≤7.0 Torr).
[e] Ref. [8] (713–833 K, 25–760 Torr).
[f] Ref. [14] (1147–1230 K, ≈1.5 bar).

value. However, with this basis set, the interaction energies between H_2O_2 and CO_2 were found to be too attractive compared to the reference coupled-cluster calculations, which would result in systematic errors in the calculations. The use of larger basis sets was found to be necessary to eliminate potential systematic bias in the interaction energy for M = CO_2 (and also for M = H_2O_2), which were computationally too demanding.

The third-body effects on the falloff curve of the rate constants are evaluated. The falloff curve is generally represented using the formula proposed by Troe and co-workers [36–38]; there exist several variants and the asymmetric expression described in the work of Gilbert et al. [37] is employed here. The curve is characterized by the center broadening factor, F_{cent}, the weak-collision component of which is approximately represented as $F_{cent,wc} \approx \max\{\beta_c^{0.14}, 0.64(\pm 0.03)\}$ [38]. This gives $F_{cent,wc}$ = 0.67–0.83 and 0.64–0.70 at 750 and 1500 K, respectively. Therefore, the falloff curves are expected to not significantly differ between the third-body molecules. This is demonstrated in Fig. 4 where the rate constants calculated by solving the master equation are shown as doubly reduced falloff curves. The falloff curves for the seven third-body molecules are almost identical among each other and can be represented by the F_{cent} values of 0.56 and 0.45 at temperatures of 750 and 1500 K, respectively, or the temperature dependent expression of

$$F_{cent} = 0.7 \exp(-T/3400\,\mathrm{K}) \quad (8)$$

derived from the falloff curves for M = Ar calculated at several temperatures ranging from 500 to 2000 K. Using these optimal values of F_{cent}, the calculated pressure-dependent rate constants are reproduced by the falloff expression [37] within errors of at most ±15%.

Finally, the multicomponent third-body effects [39–41] on the pressure-dependent rate constants are examined. Due to the different efficiencies of collisions with bath gas molecules, the rate constants in the falloff region and low-pressure limit deviate from the traditional, pressure-based linear mixture rule (LMR,P) [41]. This effect is illustrated in Fig. 5, where the rate constants calculated at pressures ranging from 0.1 to 100 bar for the bath gas mixtures consisting of N_2 and H_2O, $k(N_2,H_2O)$, relative to those for the pure N_2 bath gas, $k(N_2)$, are plotted as a function of the mole fraction of H_2O, $x(H_2O)$, in the bath gas mixture. The rate constants are calculated by solving the master equations that explicitly include the energy transfer probabilities for the collisions with the individual bath-gas components. The dashed straight lines represent the rate constants estimated by LMR,P as $k(N_2,H_2O) = [1 - x(H_2O)]\, k(N_2) + x(H_2O)\, k(H_2O)$. They are close to the master equation results at low pressures but deviate from them at high pressures. In the same way, the rate constants are calculated over 0.1–100 bar

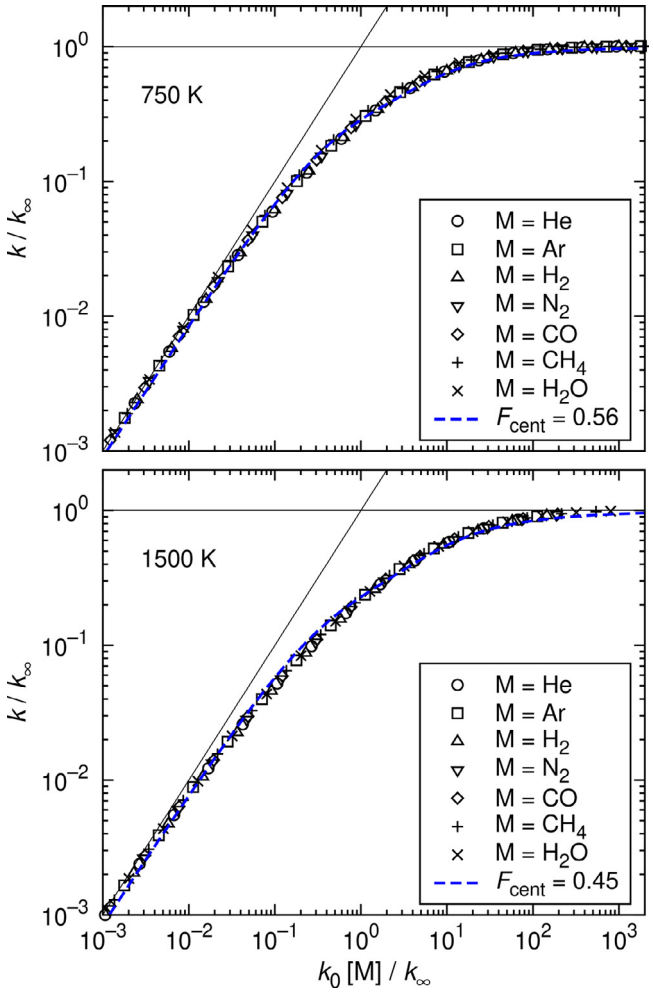

Fig. 4. Doubly reduced falloff curves of the calculated rate constants (symbols) at 750 (top) and 1500 (bottom) K. The solid lines represent the limiting high- and low-pressure rate constants. The dashed lines are the analytical falloff curves with the optimal F_{cent}.

for possible 21 binary combinations of the third-body molecules studied, and the maximum deviations from the master equation results are listed in Table 5. The deviations are small for combinations of molecules having similar collision efficiencies but increase as the difference in k_0 for two colliders increases and can become comparable to the uncertainty in the rate constants and relative third-body efficiencies themselves. These deviations mostly

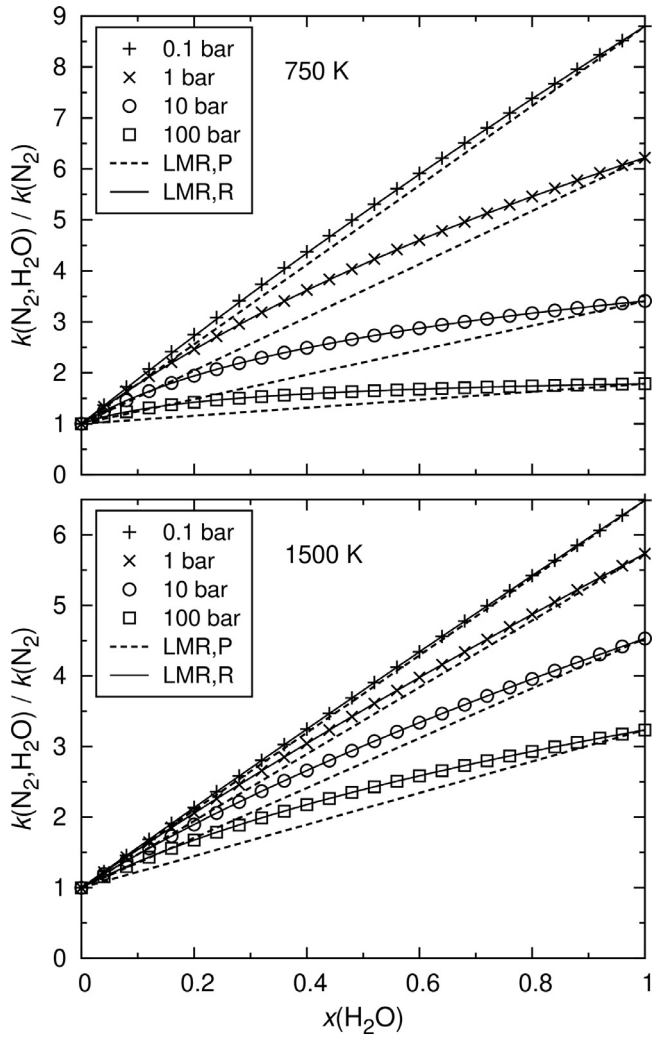

Fig. 5. Ratios of the rate constants in the N_2 and H_2O mixture bath to those in the pure N_2 bath calculated by solving the master equations (symbols) and using the linear mixture rules based on the pressure (LMR,P; dashed lines) and reduced pressure (LMR,R; solid lines) at temperatures of 750 (top panel) and 1500 (bottom panel) K and pressures of 0.1, 1, 10, and 100 bar from top to bottom.

originate from the different pressure dependence of the rate constants between the third-body molecules. The universality of the doubly reduced falloff curves (Fig. 4) for various third-body molecules indicates that the differences of the pressure dependence can be accounted for by using the reduced pressure which is proportional to k_0(M)[M]. This is equivalent to the reduced-pressure-based linear mixture rule (LMR,R) proposed by Burke and Song [41]. The rate constants estimated by LMR,R are shown in Fig. 5 as the solid curved lines, which closely reproduce the rate constants calculated by the master equation. The deviations are subtle and at most −2.6% as shown in Table 5. Therefore, the reduced-pressure-based rule is certainly a better implementation of the multicomponent third-body effects than the traditional pressure-based one.

The above observations on the falloff curves and multicomponent third-body effects are based on the energy transfer parameters and collision frequencies obtained from the trajectories. As discussed in the previous studies [32,35], the collision frequency should be consistent with the presumed energy transfer model and its parameter. In contrast, the LJ collision frequencies have been conventionally employed in master equation analyses of pressure-dependent rate constants. The use of the LJ collision frequencies

Table 5
Maximum deviations (%) of the rate constants estimated using the linear mixture rules from those calculated by solving the master equations over the pressure range 0.1−100 bar.

M_1	M_2	750 K, LMR,P	750 K, LMR,R	1500 K, LMR,P	1500 K, LMR,R
He	Ar	−0.3	−0.3	−0.2	−0.2
He	H_2	−4.1	−0.1	−1.9	−0.1
He	N_2	−3.6	−0.1	−1.1	−0.0
He	CO	−6.9	−0.3	−4.2	−0.1
He	CH_4	−20.6	−1.6	−10.0	−0.4
He	H_2O	−38.6	−2.3	−21.4	−0.1
Ar	H_2	−2.3	−0.5	−1.5	−0.5
Ar	N_2	−1.8	−0.0	−0.9	−0.2
Ar	CO	−4.4	−0.0	−3.6	−0.0
Ar	CH_4	−16.7	−0.6	−9.0	−0.0
Ar	H_2O	−34.3	−1.0	−20.1	−0.0
H_2	N_2	−0.3	−0.3	−0.1	−0.1
H_2	CO	−0.5	−0.5	−0.5	−0.4
H_2	CH_4	−7.7	−2.0	−3.5	−0.7
H_2	H_2O	−22.8	−2.6	−12.0	−0.4
N_2	CO	−0.6	−0.0	−1.0	−0.1
N_2	CH_4	−8.4	−0.9	−4.7	−0.3
N_2	H_2O	−23.9	−1.4	−14.0	−0.1
CO	CH_4	−4.7	−0.5	−1.4	−0.0
CO	H_2O	−18.2	−0.9	−7.6	−0.0
CH_4	H_2O	−5.4	−0.1	−2.9	−0.0

brings much larger variations in the parameter α (and hence β_c and F_{cent}) with respect to the third-body molecules than those presented in Table 2. In particular, the value of the parameter α exceeds 5000 cm^{-1} for M = H_2O if it is linearly scaled [32] to be consistent with the LJ collision frequency. Such a large value of α would have indicated the strong collision limit [20] and brought additional non-linearities into the multicomponent third-body effects. However, the trajectory calculations indicate that this is unlikely the case because only less than 1% of collisions resulted in the transfer of energy more than 5000 cm^{-1}. The apparent strong collision limit is an artifact arising from the use of the underestimated collision frequency [34].

4. Conclusions

The energy transfer in H_2O_2 colliding with seven different third-body molecules, M, were studied by the direct trajectory calculations on the SCS′-MP2 potential energy surfaces. The energy transfer parameter α and collision frequency Z calculated form the trajectories were used in the master equation for modeling the pressure-dependent kinetics and the third-body effects in the thermal decomposition of H_2O_2. The calculated rate constants for M = Ar and N_2 near the low-pressure limits agree well with the experimental data, but there were some deviations, up to a factor of ≈2, at high pressures (≥10 bar) and high temperature (1250 K). This calls for further theoretical investigations on the microscopic rate constants for the dissociation as well as experimental studies over extended temperature and pressure ranges. The calculated relative rate constants are consistent with the available experimental data except for M = H_2O at the low temperature where the effect of the angular momentum conservation is suggested to be important. The doubly reduced falloff curves of the pressure-dependent rate constants for seven third-body molecules fall on the same line and are found to be represented by the universal parameter F_{cent}. The effects of multicomponent bath gases were evaluated, and the mixture rule based on the reduced pressure is found to be suitable for precisely describing the pressure-dependent rate constants in mixture bath gases.

Declaration of Competing Interest

The authors declare that they have no known competing financial interests or personal relationships that could have appeared to influence the work reported in this paper.

Acknowledgment

This work was supported by JSPS KAKENHI Grant numbers 18K13709 and 20K04318.

References

[1] C.K. Westbrook, Chemical kinetics of hydrocarbon ignition in practical combustion systems, Proc. Combust. Inst. 28 (2000) 1563–1577.
[2] J.F. Griffiths, K.J. Hughes, R. Porter, The role and rate of hydrogen peroxide decomposition during hydrocarbon two-stage autoignition, Proc. Combust. Inst. 30 (2005) 1083–1091.
[3] W. Liang, C.K. Law, An analysis of the explosion limits of hydrogen/oxygen mixtures with nonlinear chain reactions, Phys. Chem. Chem. Phys. 20 (2018) 742–751.
[4] A. Miyoshi, Kinetics of autoignition: a simple intuitive interpretation and its relation to the Livengood-Wu integral, Phys. Chem. Chem. Phys. 20 (2018) 10762–10769.
[5] C.K. McLane, Hydrogen peroxide in the thermal hydrogen oxygen reaction I. Thermal decomposition of hydrogen peroxide, J. Chem. Phys. 17 (1949) 379–385.
[6] C.N. Satterfield, T.W. Stein, Homogeneous decomposition of hydrogen peroxide vapor, J. Phys. Chem. 61 (1957) 537–540.
[7] D.E. Hoare, J.B. Protheroe, A.D. Walsh, The thermal decomposition of hydrogen peroxide vapour, Trans. Faraday Soc. 55 (1959) 548–557.
[8] R.R. Baldwin, D. Brattan, Homogeneous gas-phase decomposition of hydrogen peroxide, Symp. (Int.) Combust. 8 (1961) 110–119.
[9] P.A. Giguère, I.D. Liu, Kinetics of the thermal decomposition of hydrogen peroxide vapor, Can. J. Chem. 35 (1957) 283–293.
[10] W. Forst, Second-order unimolecular kinetics in the thermal decomposition of hydrogen peroxide vapor, Can. J. Chem. 36 (1958) 1308–1319.
[11] E. Meyer, H.A. Olschewski, J. Troe, H.G. Wagner, Investigation of N_2H_4 and H_2O_2 decomposition in low and high pressure shock waves, Symp. (Int.) Combust. 12 (1969) 345–355.
[12] J. Troe, Ultravioletttspektrum und Reaktionen des HO-Radikals im thermischen Zerfall von HO, Ber. Bunsenges. Phys. Chem. 73 (1969) 946–952.
[13] C. Kappel, K. Luther, J. Troe, Shock wave study of the unimolecular dissociation of H_2O_2 in its falloff range and of its secondary reactions, Phys. Chem. Chem. Phys. 4 (2002) 4392–4398.
[14] Z. Hong, A. Farooq, E.A. Barbour, D.F. Davidson, R.K. Hanson, Hydrogen peroxide decomposition rate: a shock tube study using tunable laser absorption of H_2O near 2.5 μm, J. Phys. Chem. A 113 (2009) 12919–12925.
[15] Z. Hong, R.D. Cook, D.F. Davidson, R.K. Hanson, A shock tube study of $OH + H_2O2 \rightarrow H_2O + HO_2$ and $H_2O_2 + M \rightarrow 2OH + M$ using laser absorption of H_2O and OH, J. Phys. Chem. A 114 (2010) 5718–5727.
[16] M.B. Sajid, Et. Es-sebbar, T. Javed, C. Fittschen, A. Farooq, Measurement of the rate of hydrogen peroxide thermal decomposition in a shock tube using quantum cascade laser absorption near 7.7 μm, Int. J. Chem. Kinet. 46 (2014) 275–284.
[17] A.B.S. Alquaity, U. KC, A. Popov, A. Farooq, Detection of shock-heated hydrogen peroxide (H_2O_2) by off-axis cavity-enhanced absorption spectroscopy (OA-CEAS), Appl. Phys. B 123 (2017) 280.
[18] J. Troe, V.G. Ushakov, SACM/CT study of the dissociation/recombination dynamics of hydrogen peroxide on an ab initio potential energy surface Part II. Specific rate constants $k(E,J)$, thermal rate constants $k_\infty(T)$, and lifetime distributions, Phys. Chem. Chem. Phys. 10 (2008) 3915–3924.
[19] S.R. Sellevag, Y. Georgievskii, J.A. Miller, Kinetics of the gas-phase recombination reaction of hydroxyl radicals to form hydrogen peroxide, J. Phys. Chem. A 113 (2009) 4457–4467.
[20] J. Troe, The thermal dissociation/recombination reaction of hydrogen peroxide $H_2O_2(+M) \rightleftarrows 2OH(+M)$ III. Analysis and representation of the temperature and pressure dependence over wide ranges, Combust. Flame 158 (2011) 594–601.
[21] N.J. Brown, J.A. Miller, Collisional energy transfer in the low-pressure-limit unimolecular dissociation of HO_2, J. Chem. Phys. 80 (1984) 5568–5580.
[22] H. Hippler, H.W. Schranz, J. Troe, Trajectory calculations of intermolecular energy transfer in sulfur dioxide-argon collisions. Method and representative results, J. Phys. Chem. 90 (1986) 6158–6167.
[23] A.R. Whyte, R.G. Gilbert, A classical trajectory calculation of average energy transfer parameters for the CH_3OO + Ar system, Aust. J. Chem. 42 (1989) 1227–1234.
[24] K.F. Lim, R.G. Gilbert, Calculation of collisional-energy-transfer rates in highly excited molecules, J. Phys. Chem. 94 (1990) 72–77.
[25] G. Lendvay, G.C. Schatz, Trajectory studies of collisional relaxation of highly excited CS_2 by H_2, CO, HCl, CS_2, and CH_4, J. Chem. Phys. 96 (1992) 4356–4365.
[26] V. Bernshtein, I. Oref, Intermolecular energy transfer probabilities from trajectory calculations: a new approach, J. Chem. Phys. 108 (1998) 3543–3553.
[27] J.R. Barker, R.E. Weston, Collisional energy transfer probability densities $P(E, J; E', J')$ for monatomics colliding with large molecules, J. Phys. Chem. A 114 (2010) 10619–10633.
[28] A.W. Jasper, J.A. Miller, Theoretical unimolecular kinetics for $CH_4 + M \rightleftarrows CH_3 + H + M$ in eight baths, M = He, Ne, Ar, Kr, H_2, N_2, CO, and CH_4, J. Phys. Chem. A 115 (2011) 6438–6455.
[29] A.W. Jasper, J.A. Miller, S.J. Klippenstein, Collision efficiency of water in the unimolecular reaction $CH_4 (+H_2O) \rightleftarrows CH_3 + H (+H_2O)$: One-dimensional and two-dimensional solutions of the low-pressure-limit master equation, J. Phys. Chem. A 117 (2013) 12243–12255.
[30] A.W. Jasper, K.M. Pelzer, J.A. Miller, E. Kamarchik, L.B. Harding, S.J. Klippenstein, Predictive a priori pressure-dependent kinetics, Science 346 (2014) 1212–1215.
[31] R. Conte, P.L. Houston, J.M. Bowman, Trajectory study of energy transfer and unimolecular dissociation of highly excited allyl with argon, J. Phys. Chem. A 118 (2014) 7742–7757.
[32] A. Matsugi, Collision frequency for energy transfer in unimolecular reactions, J. Phys. Chem. A 122 (2018) 1972–1985.
[33] A. Matsugi, Dissociation channels, collisional energy transfer, and multichannel coupling effects in the thermal decomposition of CH_3F, Phys. Chem. Chem. Phys. 20 (2018) 15128–15138.
[34] A. Matsugi, Origin of bath gas dependence in unimolecular reaction rates, J. Phys. Chem. A 123 (2019) 764–770.
[35] A. Matsugi, Modeling collisional transitions in thermal unimolecular reactions: successive trajectories and two-dimensional master equation for trifluoromethane decomposition in an argon bath, J. Phys. Chem. A 124 (2020) 6645–6659.
[36] J. Troe, Predictive possibilities of unimolecular rate theory, J. Phys. Chem. 83 (1979) 114–126.
[37] R.G. Gilbert, K. Luther, J. Troe, Theory of thermal unimolecular reactions in the fall-off range. II. Weak collision rate constants, Ber. Bunsenges. Phys. Chem. 87 (1983) 169–177.
[38] J. Troe, V.G. Ushakov, Revisiting falloff curves of thermal unimolecular reactions, J. Chem. Phys. 135 (2011) 054304.
[39] J. Troe, Mixture rules in thermal unimolecular reactions, Ber. Bunsenges. Phys. Chem. 84 (1980) 829–834.
[40] J.E. Dove, S. Halperin, S. Raynor, Deviations from the linear mixture rule in nonequilibrium chemical kinetics, J. Chem. Phys. 81 (1984) 799–811.
[41] M.P. Burke, R. Song, Evaluating Mixture Rules for Multi-Component Pressure Dependence: $H+O_2$ (+M) = HO_2 (+M), Proc. Combust. Inst. 36 (2017) 245–253.
[42] S. Grimme, Improved second-order Møller-Plesset perturbation theory by separate scaling of parallel- and antiparallel-spin pair correlation energies, J. Chem. Phys. 118 (2003) 9095–9102.
[43] T.B. Adler, G. Knizia, H.-J. Werner, A simple and efficient CCSD(T)-F12 approximation, J. Chem. Phys. 127 (2007) 221106.
[44] G. Knizia, T.B. Adler, H.-J. Werner, Simplified CCSD(T)-F12 methods: Theory and benchmarks, J. Chem. Phys. 130 (2009) 054104.
[45] M.J. Frisch, G.W. Trucks, H.B. Schlegel, G.E. Scuseria, M.A. Robb, J.R. Cheeseman, G. Scalmani, V. Barone, B. Mennucci, G.A. Petersson, H. Nakatsuji, M. Caricato, X. Li, H.P. Hratchian, A.F. Izmaylov, J. Bloino, G. Zheng, J.L. Sonnenberg, M. Hada, M. Ehara, K. Toyota, R. Fukuda, J. Hasegawa, M. Ishida, T. Nakajima, Y. Honda, O. Kitao, H. Nakai, T. Vreven, J.A. Montgomery Jr., J.E. Peralta, F. Ogliaro, M. Bearpark, J.J. Heyd, E. Brothers, K.N. Kudin, V.N. Staroverov, T. Keith, R. Kobayashi, J. Normand, K. Raghavachari, A. Rendell, J.C. Burant, S.S. Iyengar, J. Tomasi, M. Cossi, N. Rega, J.M. Millam, M. Klene, J.E. Knox, J.B. Cross, V. Bakken, C. Adamo, J. Jaramillo, R. Gomperts, R.E. Stratmann, O. Yazyev, A.J. Austin, R. Cammi, C. Pomelli, J.W. Ochterski, R.L. Martin, K. Morokuma, V.G. Zakrzewski, G.A. Voth, P. Salvador, J.J. Dannenberg, S. Dapprich, A.D. Daniels, O. Farkas, J.B. Foresman, J.V. Ortiz, J. Cioslowski, D.J. Fox, Gaussian 09, Revision C.01, Gaussian, Inc., Wallingford, CT, 2010.
[46] H.-J. Werner, P.J. Knowles, G. Knizia, F.R. Manby, M. Schütz, P. Celani, W. Györffy, D. Kats, T. Korona, R. Lindh, A. Mitrushenkov, G. Rauhut, K.R. Shamasundar, T.B. Adler, R.D. Amos, S.J. Bennie, A. Bernhardsson, A. Berning, D.L. Cooper, M.J.O. Deegan, A.J. Dobbyn, F. Eckert, E. Goll, C. Hampel, A. Hesselmann, G. Hetzer, T. Hrenar, G. Jansen, C. Köppl, S.J.R. Lee, Y. Liu, A.W. Lloyd, Q. Ma, R.A. Mata, A.J. May, S.J. McNicholas, W. Meyer, T.F. Miller III, M.E. Mura, A. Nicklass, D.P. O'Neill, P. Palmieri, D. Peng, K. Pflüger, R. Pitzer, M. Reiher, T. Shiozaki, H. Stoll, A.J. Stone, R. Tarroni, T. Thorsteinsson, M. Wang, M. Welborn, MOLPRO, Version 2018.2, Cardiff, UK, 2018.
[47] G.H. Peslherbe, H. Wang, W.L. Hase, Monte Carlo sampling for classical trajectory simulations, Adv. Chem. Phys. 105 (2007) 171–201.
[48] S.K. Gray, D.W. Noid, B.G. Sumpter, Symplectic integrators for large scale molecular dynamics simulations: A comparison of several explicit methods, J. Chem. Phys. 101 (1994) 4062–4072.
[49] R.G. Gilbert, S.C. Smith, Theory of Unimolecular and Recombination Reactions, Blackwell, Oxford, UK, 1990.
[50] B. Efron, R. Tibshirani, Bootstrap methods for standard errors, confidence intervals, and other measures of statistical accuracy, Stat. Sci. 1 (1986) 54–75.
[51] R.D. Johnson III, NIST Computational Chemistry Comparison and Benchmark Database, NIST Standard Reference Database Number 101, Release 21, August 2020, http://cccbdb.nist.gov/, doi:10.18434/T47C7Z.
[52] A. Miyoshi, BEx1D software, rev. 2008.10.08, 2008. http://akrmys.com/bex1d/.
[53] J. Koput, S. Carter, N.C. Handy, Potential energy surface and vibrational-ro-

tational energy levels of hydrogen peroxide, J. Phys. Chem. A 102 (1998) 6325–6330.
[54] W. Forst, Unimolecular reactions: A concise Introduction, Cambridge University Press, Cambridge, UK, 2003.
[55] M. Sangwan, E.N. Chesnokov, L.N. Krasnoperov, Reaction OH + OH studied over the 298-834 K temperature and 1-100 bar pressure ranges, J. Phys. Chem. A 116 (2012) 6282–6294.
[56] L. Monchick, E.A. Mason, Transport Properties of Polar Gases, J. Chem. Phys. 35 (1961) 1676–1697.
[57] E.A. Mason, L. Monchick, Transport Properties of Polar-Gas Mixtures, J. Chem. Phys. 36 (1962) 2746–2757.
[58] B.E. Poling, J.M. Prausnitz, J.P. O'Connell, The Properties of Gases and Liquids, 5th edn., McGraw-Hill Professional, Boston, MA, 2001.
[59] R.D. Nelson Jr., D.R. Lide, A.A. Maryott, Selected Values of Electric Dipole Moments For Molecules in the Gas Phase (NSRDS-NBS10), National Bureau of Standards, Washington, D.C., 1967.
[60] S.C. Chan, B.S. Rabinovitch, J.T. Bryant, L.D. Spicer, T. Fujimoto, Y.N. Lin, S.P. Pavlou, Energy transfer in thermal methyl isocyanide isomerization. Comprehensive investigation, J. Phys. Chem. 74 (1970) 3160–3176.
[61] J.V. Michael, M.-.C. Su, J.W. Sutherland, J.J. Carroll, A.F. Wagner, Rate constants for $H + O_2 + M \rightarrow HO_2 + M$ in seven bath gases, J. Phys. Chem. A 106 (2002) 5297–5313.
[62] G. Altinay, R.G. Macdonald, Determination of the rate constant for the $NH_2(X^2B_1) + NH_2(X^2B_1)$ recombination reaction with collision partners He, Ne, Ar, and N_2 at low pressures and 296 K. Part 1, J. Phys. Chem. A 116 (2012) 1353–1367.
[63] D.C. Tardy, B.S. Rabinovitch, Intermolecular vibrational energy transfer in thermal unimolecular systems, Chem. Rev. 77 (1977) 369–408.
[64] J. Troe, Theory of thermal unimolecular reactions at low pressures. I. Solutions of the master equation, J. Chem. Phys. 66 (1977) 4745–4757.